

## **Seismic fracture detection in the Second White Speckled Shale: Anisotropic perspectives on an isotropic workflow**

David Cho, Craig Coulombe, Scott McLaren, Kevin Johnson and Gary F. Margrave

### **ABSTRACT**

Seismic methods for fracture detection typically require an azimuthal analysis of the recorded wavefield. However, conventional data acquisition practices often provide insufficient azimuthal and offset coverage for proper application of azimuthal techniques. Therefore in most cases, alternative methods must be used for fracture detection.

This study investigates the ability of seismically derived isotropic properties in the delineation of fractures within the Second White Speckled Shale. Fracture systems with structural controls were identified through attributes that are sensitive to changes in the structure of the seismic image. In addition, elastic properties were derived from the seismic measurements to investigate the conditions that control fracture formation in a given stress environment. Travel-times through anisotropic models were also analyzed to determine the propagation response in the presence of fractures. The analysis yields a set of attributes that are sensitive to fractures and are used in the reduction of uncertainty for the delineation of the associated fracture systems.

### **INTRODUCTION**

The Second White Speckled Shale (SWS) is an Upper Cretaceous marine mudstone deposited throughout the Alberta basin. It is believed to be a regionally continuous hydrocarbon system serving as both a source rock and as a reservoir rock. Production from the SWS is attributed to preferential fracturing that creates sufficient room for storage and permeable pathways for fluid flow, providing the conditions for a self-sourcing hydrocarbon system. Exploration in the SWS therefore amounts to the detection of fractured zones within the formation.

Direct methods for the detection of fractures require an azimuthal analysis of the seismic wavefield, where the presence of aligned fractures introduce anisotropy in the medium and manifest as azimuthal variations in the seismic response. Reflection amplitudes can be inverted for fracture parameters (i.e. Downton and Roure, 2010), however the large number of parameters required for the description of anisotropic media requires sufficient azimuthal and offset sampling of the wavefield to provide a well-posed inverse problem. In most situations, the data requirements for inversion are not fulfilled and therefore inhibit the use of azimuthal analysis for fracture characterization. Alternative means for fracture detection are then necessary given the limitations in resource availability.

In this study, we investigate the ability of seismically derived parameters from an isotropic workflow in the delineation of fracture systems in the SWS. The study consists of a multi-attribute analysis which includes the use of a pattern recognition algorithm to identify fracture patterns from the seismic image, an investigation of the P-wave response

of an anisotropic fracture model, optimal conditions for fracturing based on failure criteria and an analysis of the residual moveout due to anisotropy.

### STRESS HISTORY AND FRACTURE ORIENTATIONS

Fractures that form in a confined stress environment are relatively well behaved, where the fracture plane is oriented at an acute angle to the maximum principle stress direction (Coulomb, 1773). Therefore, knowledge of the stress history can be used to constrain the orientation of the fractures. The main control for the stress history of the Alberta basin is the compressive forces that are applied in the formation of the Rocky Mountains as illustrated in Figure 1.

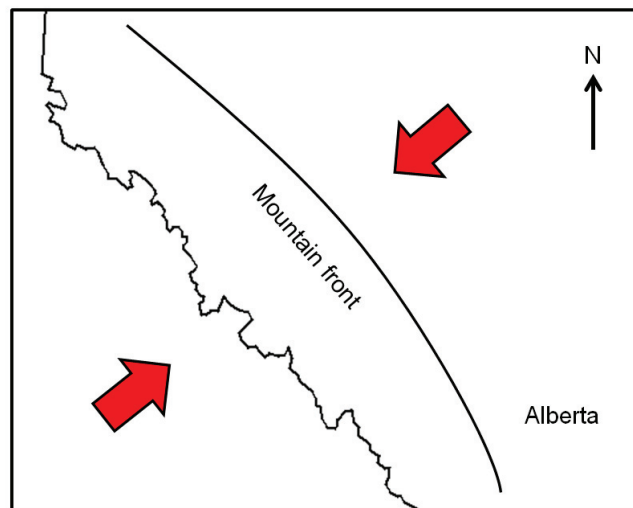


FIG. 1. Map illustrating the direction of the compressive forces in the formation of the Rocky Mountains in Alberta.

The stress history of the SWS can be classified into various stress regimes under which fracture formation would have been possible. It began with the Laramide Orogeny which occurred approximately between 40-70 Ma and at the time of deposition of the SWS. The stress regime then changes upon the relaxation of the basin and with the additional deposition of post-Cretaceous sediments. During the Laramide Orogeny, compression of the basin resulted in a thrust faulting stress regime. The maximum horizontal stress,  $\sigma_H$  is the maximum principle stress and is oriented orthogonal to the mountain front. The vertical stress,  $\sigma_V$  is the minimum principle stress (Figure 2a). The resulting fracture planes would have an orientation that is parallel to the mountain front. As the basin relaxed and additional deposition occurred, the SWS would enter a strike-slip faulting or a normal faulting stress regime depending on the rate of relaxation and deposition. It is likely that both of these regimes were encountered throughout its stress history. In the strike-slip faulting stress regime, the maximum principle stress remains  $\sigma_H$  and the intermediate principle stress becomes  $\sigma_V$  (Figure 2b). The resulting fracture planes would have an orientation that is at an acute angle to the normal of the mountain front. In a normal faulting stress regime, the maximum principle stress is  $\sigma_V$  and the intermediate principle stress is  $\sigma_H$  (Figure 2c). The resulting fracture planes would have an orientation that is orthogonal to the mountain front. Throughout the paper, the various

fracture orientations are referenced in regards to the stress regime under which it was formed.

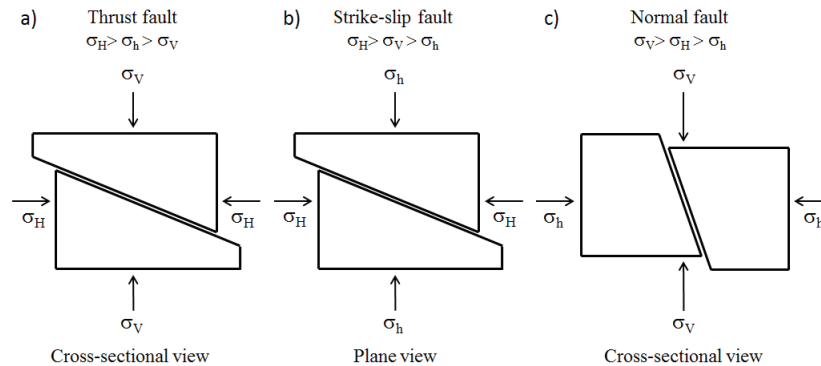


FIG. 2. Fracture orientation for various stress regimes.

Figure 3 provides evidence for two of the expected fracture orientations. Figure 3a shows a map of a pool in the SWS where the green points indicate the various well locations. The associated pressure data demonstrates excellent pressure communication between the wells and therefore suggests a permeable pathway or fractures that are oriented parallel to the mountain front. Figure 3b shows a 60 degree dipping fracture from a core sample in the same area. This suggests that the fracture was formed in a normal faulting stress regime where the maximum principle stress is vertical.

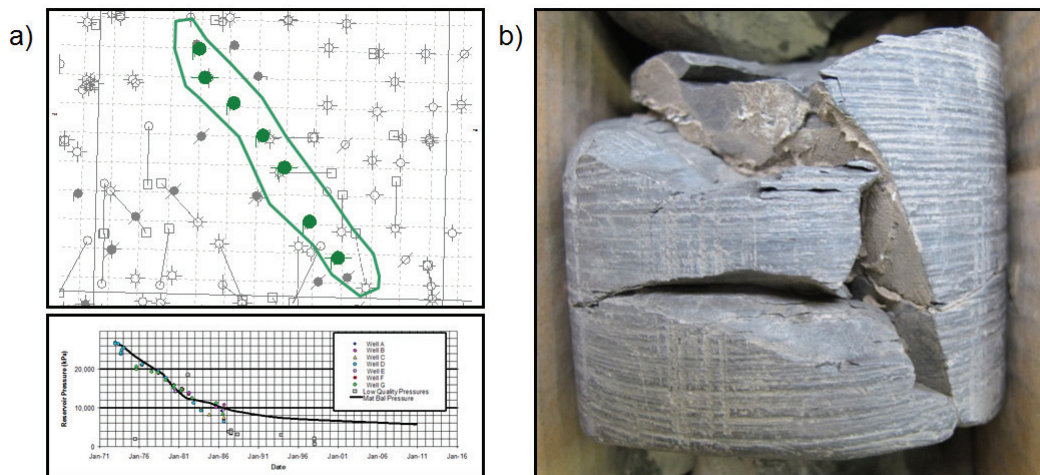


FIG. 3. Evidence of two expected fracture orientations that show a) pressure communication between the wells within a SWS pool, suggesting a permeability pathway parallel to the mountain front and b) a 60 degree dipping fracture that formed in a normal faulting stress regime.

In this study, the detection of the thrust fractures is handled separately from the strike-slip and normal fractures. The thrust fractures were formed during the compression of the basin and are accompanied by structural changes in areas that are likely to be fractured. Therefore, these features can be extracted directly from the seismic image using attributes that are sensitive to structural changes. The strike-slip and normal fractures were likely

formed as a result of its elastic properties being within the conditions for failure under a given stress regime. Therefore an inversion for the elastic properties is performed to identify areas that are favourable for fracturing.

### THRUST FRACTURE DETECTION

Since the thrust fractures are believed to be accompanied by structural deformation, seismic attributes that highlight structural changes were used to identify areas that are likely to be fractured. The Ant-Tracking workflow was chosen due to its ability to single out specific features in the seismic image. Various steps are involved in the workflow which include structural smoothing, edge detection and Ant-Tracking. The structural smoothing step applies an edge preserving smoother to the input seismic in order to enhance reflector continuity while preserving discontinuous events. Next, the edge detection algorithm detects all discontinuities that disrupt reflector continuity. Finally, the Ant-Tracking algorithm extracts features within the edge detection volume that exhibit fault-like behaviour. It uses principles from ant colony systems to extract trends in a noisy data environment that exhibit characteristics in terms of consistency in dip, azimuth, planarity and spatial continuity. Filters can also be applied to extract only desired orientations. Since the features that are of interest are thrust fractures, events that are aligned parallel to the mountain front were tracked to provide an image that highlights the areas with an increased likelihood for thrust fractures to form. Figure 4 shows the image at the various stages of the Ant-Tracking workflow.

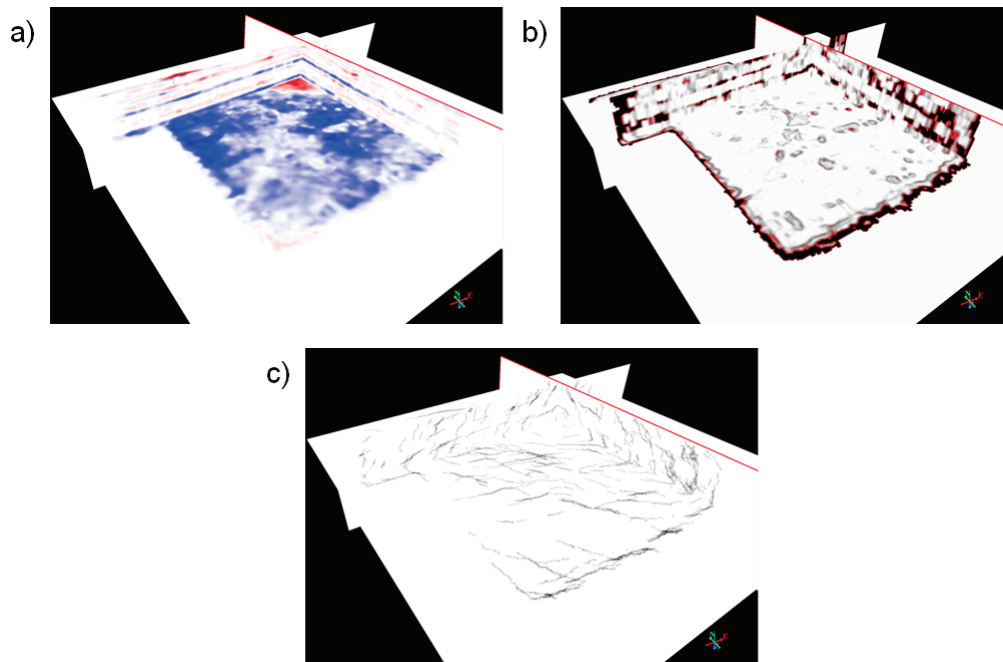


FIG. 4. Images at each step of the Ant-Tracking workflow. a) Structurally smoothed seismic, b) edge detection (variance) and c) Ant-Tracking.

### STRIKE-SLIP AND NORMAL FRACTURE DETECTION

The strike-slip and normal fractures are not believed to have formed in conjunction with structural changes. Therefore, the detection of these fractures is achieved through an

investigation into the elastic properties that control failure. To determine the elastic properties, an amplitude variation with offset (AVO) inversion was performed to extract the P- and S-wave velocities and density. Subsequently, the constitutive relations were applied for the transformation to geomechanical properties that are important in fracture mechanics.

### Hudson's penny shaped crack model

In order to investigate the response of a fractured medium, we make use of Hudson's penny shaped crack model. Hudson (1981) derived expressions for the representation of a medium containing aligned penny shaped inclusions as shown in Figure 5.

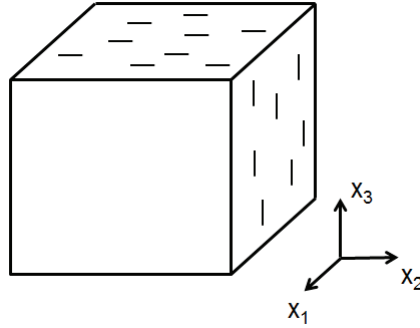


FIG. 5. Aligned penny shaped inclusions in an isotropic background medium.

The effective elastic stiffness parameters of the medium are given by

$$C_{ij}^{(eff)} = C_{ij}^{(0)} + C_{ij}^{(1)} + C_{ij}^{(2)} \quad (1)$$

where  $C_{ij}^{(0)}$  represents the elastic stiffness of the isotropic background and  $C_{ij}^{(1)}$  and  $C_{ij}^{(2)}$  represent the first and second order perturbations due to the inclusion of the penny shaped cracks respectively. For dry cracks, the first and second order perturbations are functions of the crack density,  $\varepsilon$  and the Lamé parameters,  $\lambda$  and  $\mu$ .

### Velocity variation with crack density

The vertical P-wave velocity can be extracted from an AVO inversion and is represented by the  $C_{33}$  component of the elastic stiffness tensor. Using Hudson's penny shaped crack model, we can investigate the vertical P-wave response of a fractured medium by the addition of the perturbation terms as given in equation 1. Consider a medium containing a series of vertical penny shaped cracks aligned in the  $x_2$ - $x_3$  plane as in Figure 5. Assuming that  $\varepsilon$  is small, we can neglect the second order term in equation 1 and the resulting effective vertical P-wave velocity is given by

$$V_p^{(eff)} = \sqrt{\frac{C_{33}^{(eff)}}{\rho}} = \sqrt{\frac{1}{\rho} \left( \lambda + 2\mu - \frac{4\lambda^2(\lambda + 2\mu)}{3\mu(\lambda + \mu)} \varepsilon \right)}, \quad (2)$$

where  $\rho$  is the density of the medium. Note that the term containing  $\varepsilon$  is always negative, therefore an increase in crack density results in a decrease in the vertical P-wave velocity.

Using this result, we can identify zones with a decrease in the vertical P-wave velocity as an indicator for the presence of fractures.

### Brittleness

In discussing how a material fails under stress, the term brittleness has been used extensively in recent years. A material can be defined as brittle if when subjected to stress, it fails without significant deformation or strain. Rickman et al. (2008) provided a definition for brittleness using elastic properties of the medium, namely the Poisson's ratio,  $\nu$  and the Young's modulus,  $E$ . In their definition,  $\nu$  controls the ability to fail under stress and  $E$  controls the ability to maintain a fracture. The brittleness of a material then increases with a decreasing  $\nu$  and an increasing  $E$  which is illustrated in Figure 6.

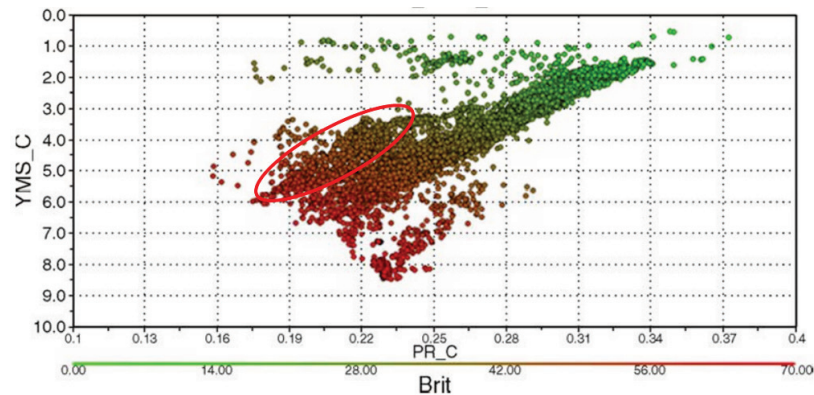


FIG. 6. Brittleness as a function of the Poisson's ratio and Young's modulus (Rickman et al., 2008).

The context under which Rickman et al. (2008) defined brittleness was in a hydraulic fracturing environment. The relationship between  $\nu$  and the ability to fail under stress can be understood in terms of the transverse release in energy due to an applied stress.  $\nu$  describes the amount of transverse deformation that is possible for a material given an applied stress. Therefore, materials with a high value of  $\nu$  can more easily release the accumulated energy through transverse deformation whereas materials with a low value for  $\nu$  cannot. The accumulated energy in a low  $\nu$  material then works to break the atomic bonds of the material resulting in failure. The relationship between  $E$  and the ability to maintain a fracture can be understood through the closure stress equation, which is given by

$$\sigma_{closure} = \frac{\nu}{1-\nu} \sigma_V + \frac{E}{1-\nu^2} (e_{xx} + \nu e_{yy}), \quad (3)$$

where  $e_{xx}$  and  $e_{yy}$  are the strains in the  $x$  and  $y$  directions respectively. Since the objective in hydraulic fracturing is to create open fractures for fluid flow, a material with a high closure stress is desired and can be achieved through an increase in  $E$  according to equation 3. The situation for natural fractures however, is different from the hydraulic fracturing case and is discussed in the following section.

## Elastic properties and natural fractures

The Coulomb failure criterion can be used to understand the conditions under which a material will fail under stress. It states that when the applied stresses exceed the critical strength of a material, failure will occur. This criterion can be illustrated using a Mohr diagram as in Figure 7. The main components of the Mohr diagram are the Mohr circle and the failure envelope. The size of the Mohr circle is controlled by the deviatoric stress, which is the difference between the maximum and minimum principle stresses. The position of the failure envelope is determined by the uniaxial compressive or tensile strength of the material where the two are related through a scalar quantity.

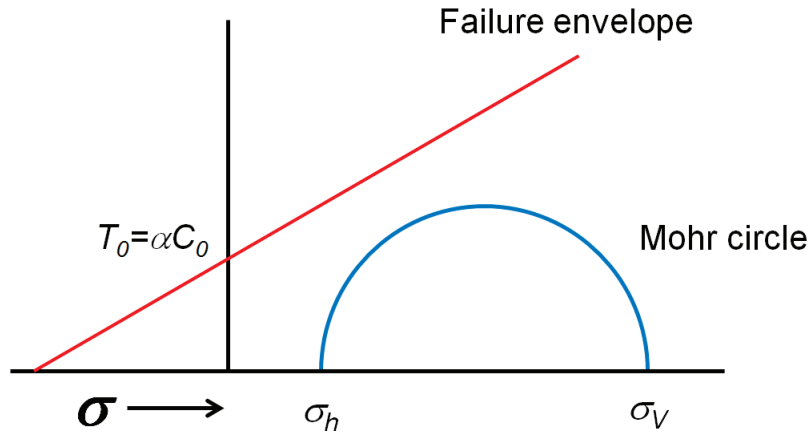


FIG. 7. Mohr diagram for failure analysis.

Failure occurs when the Mohr circle touches the failure envelope, therefore the size of the Mohr circle and the position of the failure envelope determine the conditions under which a material will fail. In searching for the optimal conditions for failure, we would seek ways in which we can increase the size of the Mohr circle and lower the position of the failure envelope. In the following, we investigate the relationship between these two components of the Mohr diagram and the elastic properties of a material.

Consider the uniaxial strain equation given by

$$\sigma_h = \frac{\nu}{1-\nu} \sigma_V, \quad (4)$$

where  $\sigma_h$  is the minimum horizontal stress. It states that for a given value of the vertical stress, the minimum horizontal stress is a function of  $\nu$ . As  $\nu$  decreases, the value of  $\sigma_h$  also decreases, resulting in a larger Mohr circle. Therefore, a material with a low  $\nu$  is more easily fractured, which is consistent with the results of Rickman et al. (2008).

Now consider an experiment as illustrated in Figure 8 where a crack of length  $2c$  is embedded in a rock specimen with the specified dimensions. A mass is attached to one end of the rock specimen containing the crack via a frictionless pulley that applies a tensile stress.

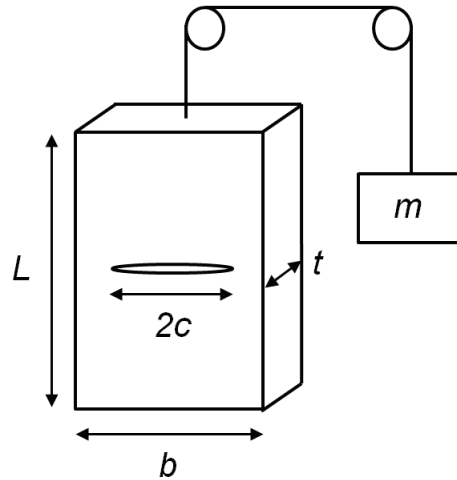


FIG. 8. Griffith crack growth experiment.

Griffith (1920) used thermodynamic arguments to derive a criterion under which crack growth is possible under an applied load. The result for a three-dimensional penny shaped crack is given by

$$T^* = \sqrt{\frac{\pi\gamma E}{4(1-\nu^2)c}}, \quad (5)$$

where  $\gamma$  is the surface energy per unit area and  $T^*$  is the critical tensile stress required to initiate crack growth. Note that the Coulomb failure criterion as discussed above and the criterion for crack growth as given by Griffith are based on two fundamentally different principles. The Coulomb criterion is based on a critical strength of a material and the Griffith criterion was derived from energy principles. However, equation 5 still provides insight as to the relationship between the stress that is required to achieve failure and the elastic properties of a material. The Griffith criterion suggests that a decrease in  $E$  will result in a decrease in the critical tensile stress required for crack growth. Therefore, a decrease in  $E$  amounts to a lowering of the failure envelope in the Mohr diagram. Note that this result is opposite from that of Rickman et al. (2008). In the hydraulic fracturing case, a high  $E$  is desired for increasing the closure stress to maintain an open fracture. In the case of natural fractures, a low  $E$  is desired since it represents a material that is more easily fractured under a set of given stress conditions. Therefore in the description of natural fractures, the term brittleness requires an alternative definition from that of Rickman et al. (2008).

In addition, consider the constitutive relation as given by

$$E = 3K(1 - 2\nu), \quad (6)$$

where  $K$  represents the bulk modulus of a material. For a constant value of  $K$ , equation 6 is linear and a decrease in  $\nu$  is necessarily accompanied by an increase in  $E$  as can be seen in Figure 6. A decrease in  $E$  can then be achieved by lowering the value of  $K$ .

Therefore, the points as outlined by the red circle in Figure 6 represent the optimal conditions for natural fractures to occur in a given stress environment.

### Travel-time anisotropy

Figure 9 shows two NMO corrected azimuthal offset gathers with the corresponding event of interest outlined by the red box. Each panel represents a single azimuth from zero to 180 degrees measured clockwise from North. The images were generated by increasing the bin size to achieve a more complete sampling of the offset and azimuth distribution to investigate the presence of any directional variations in the seismic response.

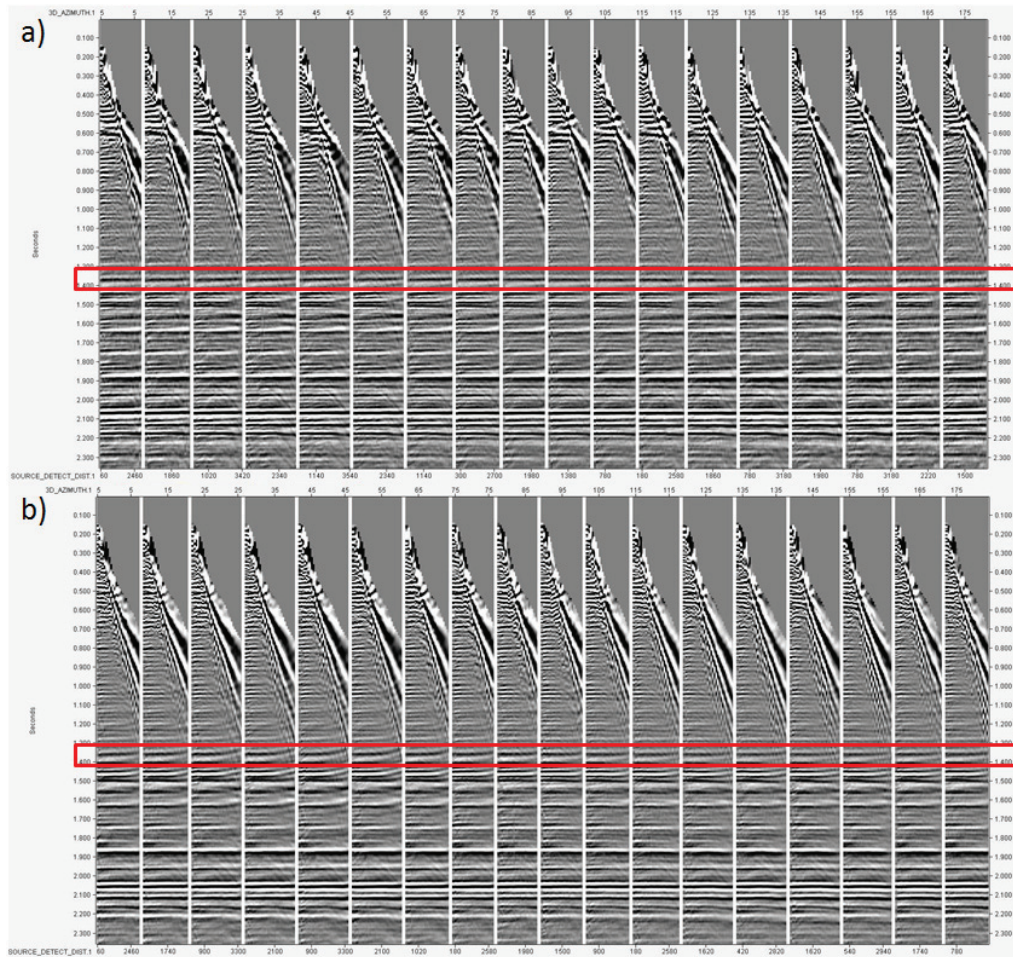


FIG. 9. NMO corrected azimuthal offset gathers for an area where fractures a) do not exist and b) exist. The azimuth is measured clockwise from North.

Figure 9a represents an area where fractures are not believed to be present. The reflection event as outlined does not demonstrate any anisotropic effects in offset or azimuth. Figure 9b however, demonstrates both an offset and azimuthal variation in the travel-time response. The event exhibits a residual moveout that varies as a function of the source receiver azimuth. A maximum curvature is observed at approximately 45

degrees and a minimum curvature at 135 degrees. In the following, we attempt to find a model that is capable of reproducing the observations in Figure 9b.

The curling up of a reflection event is typically indicative of a transversely isotropic medium with a vertical axis of symmetry (VTI). This effect is due to the inability of the isotropic migration algorithm to properly image anisotropic events. Using Hudson's penny shaped crack model, we first create a VTI medium by inserting cracks in the  $x_1$ - $x_2$  plane and further simulate aligned fractures by inserting cracks in the  $x_2$ - $x_3$  plane as illustrated by Figure 10. The resulting medium exhibits an orthorhombic symmetry.

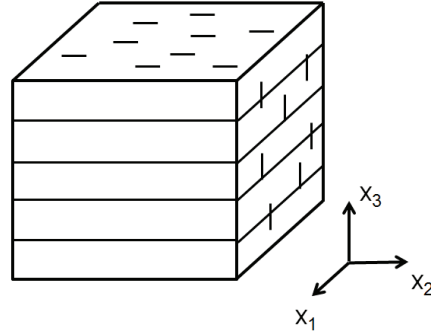


FIG. 10. A VTI medium with aligned fractures. The resulting medium has an orthorhombic symmetry.

In generating the travel-time associated with seismic wave propagation through an orthorhombic medium, we use a linearized equation for the quasi P-wave group velocity derived by Daley and Krebs (2006), which is given by

$$\frac{1}{V^2(\vec{N})} \approx \frac{N_1^2}{A_{11}} + \frac{N_2^2}{A_{22}} + \frac{N_3^2}{A_{33}} - \frac{E_{12}N_1^2N_2^2}{A_{11}A_{22}} - \frac{E_{13}N_1^2N_3^2}{A_{11}A_{33}} - \frac{E_{23}N_2^2N_3^2}{A_{22}A_{33}},$$

$$E_{12} = 2(A_{12} + 2A_{66}) - (A_{11} + A_{22}),$$

$$E_{13} = 2(A_{13} + 2A_{55}) - (A_{11} + A_{33}),$$

$$E_{23} = 2(A_{23} + 2A_{44}) - (A_{22} + A_{33}), \quad (7)$$

where  $\vec{N}$  represents a unit vector along the direction of the raypath and  $A_{ij}$  represents the density normalized elastic stiffness parameters with  $i$  and  $j$  running from 1 to 3. Also, note that the  $A_{ij}$ 's represent the effective parameters as given by Hudson's penny shaped crack model. The resulting wavefront through the orthorhombic medium can be generated using equation 7 and is illustrated in Figure 11a. In addition, Figure 11b shows the NMO corrected travel-time curves for waves propagating in a direction that is orthogonal and parallel to the fracture plane. Note the difference in the travel-time response due to the presence of the aligned fractures.

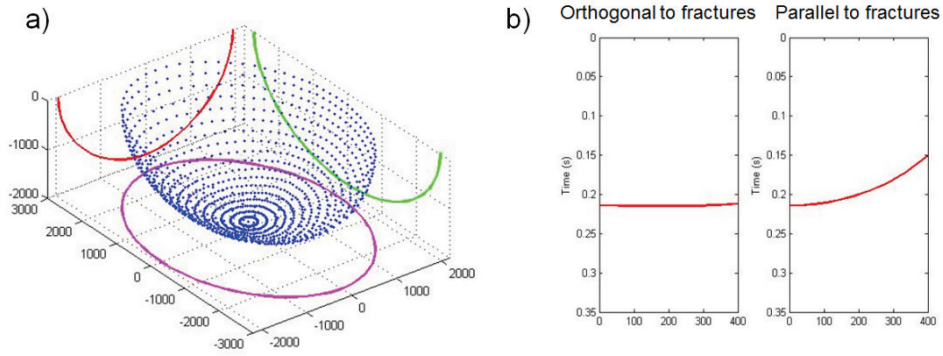


FIG. 11. a) Wavefront associated with wave propagation through an orthorhombic medium and b) NMO corrected travel-time curves for propagation directions orthogonal and parallel to fractures.

Next, we compare the modelled travel-time response to the field observations of Figure 9b. The maximum curvature event corresponds to wave propagation parallel to the fractures and the minimum curvature event corresponds to wave propagation orthogonal to the fractures as illustrated in Figure 12.

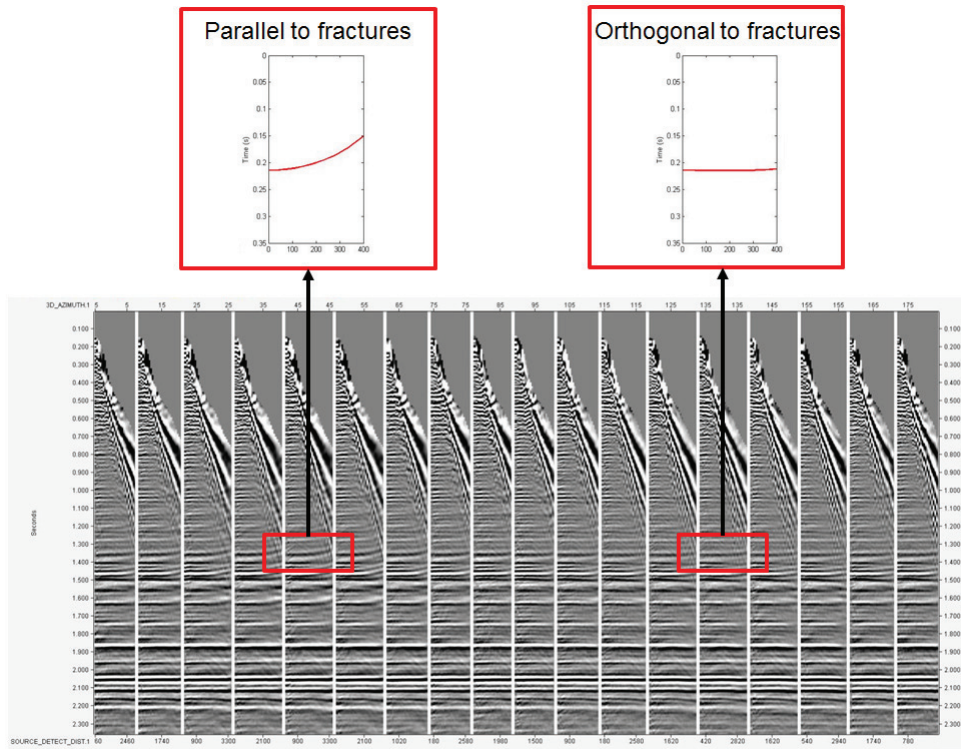


FIG. 12. Comparison of the travel-time response for modelled data and observed data.

This states that the observed azimuthal anisotropy could be the result of a VTI medium with a set of aligned fractures. In addition, the results suggest that the fractures are oriented at approximately 45 degrees or orthogonal to the mountain front, which is the expected orientation for any open fractures in the current stress regime where the maximum horizontal stress is orthogonal to the mountain front.

In addition, the results also suggest that an increase in VTI anisotropy results in an increase in fracturing. To examine this result, we investigate the effect of an increasing VTI anisotropy on the corresponding  $\nu$  associated with the medium. Again, using Hudson’s penny shaped crack model, we can generate a VTI medium by inserting cracks in the horizontal plane. The resulting  $\nu$  associated with the VTI medium can be calculated using

$$\nu_{31} = \nu_{32} = \frac{C_{12}C_{23} - C_{22}C_{13}}{C_{11}C_{22} - C_{12}^2} \quad (8)$$

where the  $C_{ij}$ ’s are the effective elastic stiffness parameters as given by Hudson’s penny shaped crack model. The resulting  $\nu$  as a function of crack density or degree of VTI anisotropy is shown in Figure 14.

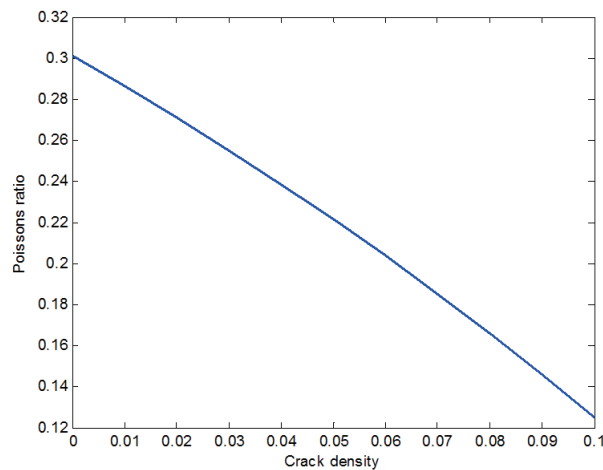


FIG. 14. Poisson’s ratio as a function of crack density or degree of VTI anisotropy.

Note that  $\nu$  decreases as the crack density or degree of VTI anisotropy increases. This is consistent with the previous discussion on how low values of  $\nu$  result in more favourable conditions for failure under a given stress environment.

In an isotropic workflow where the individual azimuths are not considered independently, all azimuthal effects will be averaged out. However, the offset response is preserved and can be used to identify areas of increased VTI anisotropy. Therefore, a residual moveout measurement due to VTI anisotropy can be used to identify areas that are more likely to be fractured.

### Fracture attributes

Given the above analysis, four attributes are used in the identification of the strike-slip and normal fractures. These include the P-wave velocity, Poisson’s ratio, Young’s modulus and a residual moveout measurement extracted from the offset gathers. The elastic properties are obtained through an AVO inversion and the residual moveout measurement consists of a time difference between the near and far offsets. Figure 15 shows the results for the various attributes.

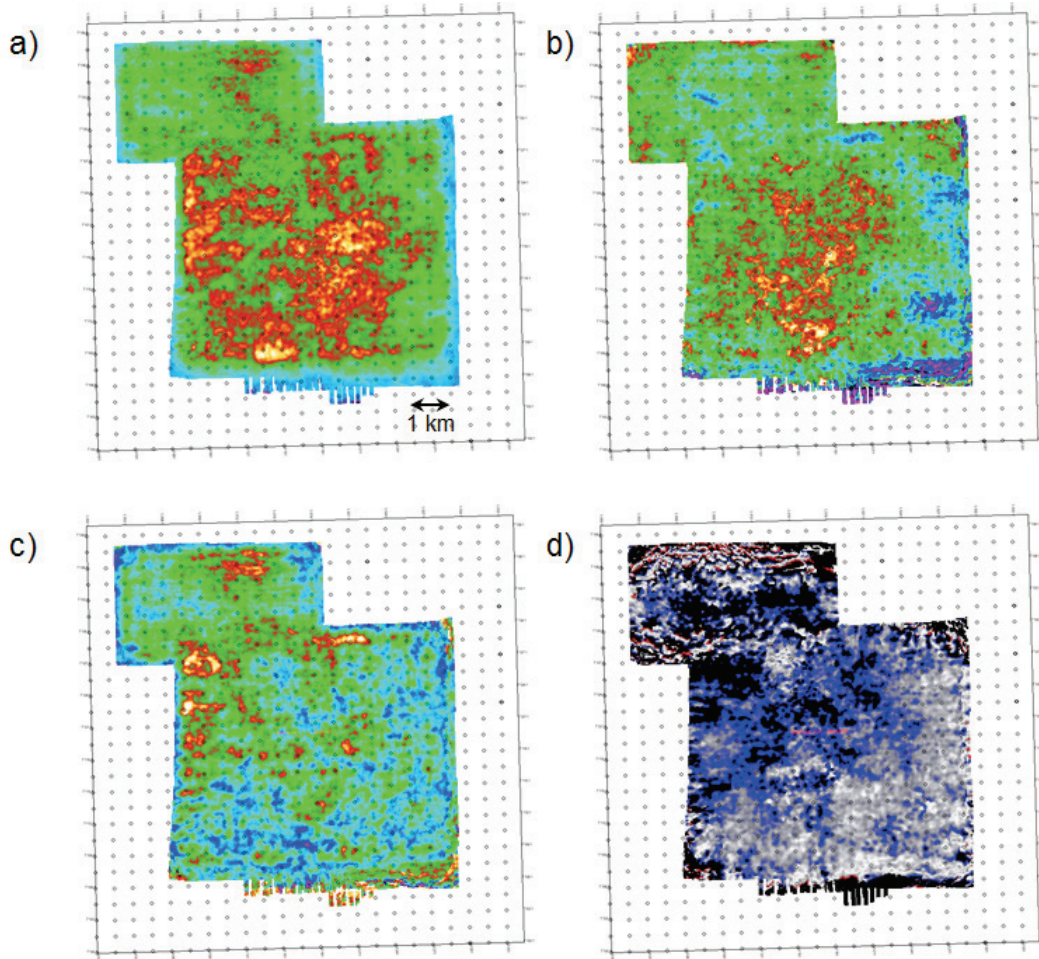


FIG. 15. Attribute maps for a) P-wave velocity, b) Poisson's ratio, c) Young's modulus and d) residual moveout. Hot colors represent low values for a) to c) and dark colors represent large residual moveout values for d).

### MULTI-ATTRIBUTE MAP

In the detection of fractures in the SWS, we implement a multi-attribute analysis to identify areas that are most favourable for fracturing based on structural information and elastic properties of the medium. The above analysis provides possible responses due to the presence of fractures. However, the responses are non-unique and could be the result of phenomenon that has not been considered. Therefore, in reducing the uncertainty associated with the non-uniqueness issue, we can combine all the attributes to provide an image that represents areas that are most likely to be fractured.

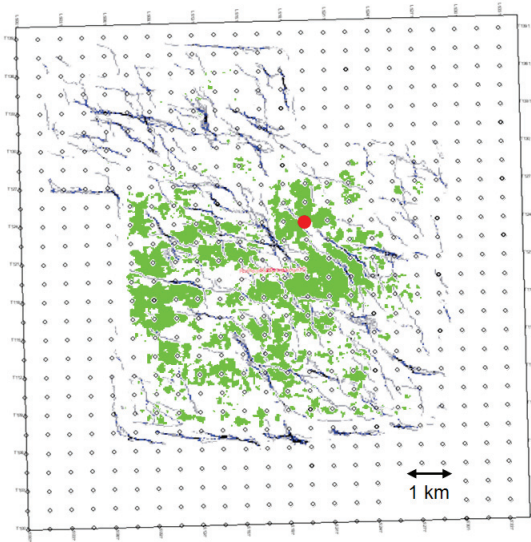


FIG. 16. Multi-attribute map for fracture detection in the SWS.

Figure 16 shows the multi-attribute map where threshold values were used to flag areas that fit a certain criteria for the strike-slip and normal fracture attributes. In addition, the Ant Tracking results were overlaid for the identification of areas with an increased likelihood for thrust fractures to form. The red dot indicates the location of a producing well within the survey and suggests that the proposed methodology was able to identify a zone where fractures are known to exist.

## CONCLUSIONS

Fractures in the SWS were identified through a multi-attribute analysis which includes structural attributes extracted from the seismic image, elastic properties extracted through an AVO inversion process and travel-time anisotropy effects. The structural attributes identified areas with an increased likelihood for the formation of fractures related to a thrust faulting stress regime. The elastic properties identified areas that were within the optimal conditions for failure under a strike-slip and normal faulting stress regime. In addition, travel-time anisotropy was used to identify areas of increased VTI anisotropy that are more favourable for fracturing.

In situations where the seismic data is not in the proper condition for azimuthal analysis, alternative means for fracture detection are possible. Additional information concerning fractures can be extracted from conventional isotropic seismic analysis techniques and used to reduce uncertainty in the detection of subsurface fractures.

## ACKNOWLEDGEMENTS

The authors thank Vermilion Energy for permission to publish this work and ARCIS for permission to show the data. Also thanks to Jiwu Lin and Greg Cameron from WesternGeco for the processing efforts associated with this study.

## REFERENCES

- Coulomb, C. A., 1773, Application of the rules of maxima and minima to some problems of statics related to architecture: Acad. Roy. Sci. Mem. Math. Phys., 7, 343-82.
- Daley, P. F., and Krebs, E., 2006, Quasi-compressional group velocity approximation in a weakly anisotropic orthorhombic medium: Journal of Seismic Exploration, No. 14, 319–334.
- Downton, J., Roure, B., 2010, Azimuthal simultaneous elastic inversion for fracture detection: 80th Annual International Meeting, SEG, Expanded Abstracts, 263-267.
- Griffith, A. A., 1920, The phenomena of flow and rupture in solids: Phil. Trans. Roy. Soc. Lond. Ser. A, 221, 163-98
- Hudson, J. A., 1981, Wave speeds and attenuation of elastic waves in material containing cracks: Geophysical Journal of the Royal Astronomical Society, 64, 133–150.
- Rickman, R., Mullen, M., Petre, E., Grieser, B., and Kundert, D., 2008, A practical use of shale petrophysics for stimulation design optimization: All shale plays are not clones of the Barnett shale, SPE 115258.